npj | Computational Materials

www.nature.com/npjcompumats

ARTICLE OPEN

Accelerated discovery of a large family of quaternary chalcogenides with very low lattice thermal conductivity

Koushik Pal[1✉], Yi Xia[1], Jiahong Shen[1], Jiangang He[1], Yubo Luo[2], Mercouri G. Kanatzidis[2] and Chris Wolverton[1✉]

The development of efficient thermal energy management devices such as thermoelectrics and barrier coatings often relies on compounds having low lattice thermal conductivity (κ_l). Here, we present the computational discovery of a large family of 628 thermodynamically stable quaternary chalcogenides, AMM′Q_3 (A = alkali/alkaline earth/post-transition metals; M/M′ = transition metals, lanthanides; Q = chalcogens) using high-throughput density functional theory (DFT) calculations. We validate the presence of low κ_l in these materials by calculating κ_l of several predicted stable compounds using the Peierls–Boltzmann transport equation. Our analysis reveals that the low κ_l originates from the presence of either a strong lattice anharmonicity that enhances the phonon-scatterings or rattler cations that lead to multiple scattering channels in their crystal structures. Our thermoelectric calculations indicate that some of the predicted semiconductors may possess high energy conversion efficiency with their figure-of-merits exceeding 1 near 600 K. Our predictions suggest experimental research opportunities in the synthesis and characterization of these stable, low κ_l compounds.

npj Computational Materials (2021)7:82 ; https://doi.org/10.1038/s41524-021-00549-x

INTRODUCTION

An important focus in materials science research has been to discover hitherto unknown materials with properties that might hold the keys to solving the most pressing problems in renewable energy, energy harvesting, or semiconductor power electronics. The augmentation of new materials discovery and the prediction of their properties have been accelerated by the advent of advanced computer algorithms coupled with high-throughput (HT) screening methods[1–10] using accurate quantum mechanical calculations based on density functional theory (DFT). In the recent past, several computational predictions have led to the successful synthesis of new solid-state compounds in a variety of chemistry and structure types in the family of half-Heuslers[9,10], double half-Heuslers[11], electrides[12], AB_2X_4-based chalcogendes[13], and rocksalt-based compounds[14].

Crystalline solids with extreme thermal transport properties are technologically important for the efficient management of thermal energy[15]. While materials with high lattice thermal conductivity (κ_l) are used in microelectronic devices for heat dissipation, materials with low κ_l are used in thermal barrier coatings[16], thermal data-storage devices[17], and high-performance thermoelectrics (TEs)[18,19] which can convert heat into electrical energy. The conversion efficiency of the TEs is defined by the figure-of-merit (ZT):

$$ZT = S^2\sigma T/(\kappa_e + \kappa_l), \tag{1}$$

where S, σ, κ_e, and κ_l are the Seebeck coefficient, electrical conductivity, electronic thermal conductivity, and lattice thermal conductivity, respectively. Engineering the electronic band structures of crystalline compounds that already possess low κ_l has emerged to be a very popular strategy to increase the ZT. Therefore, crystalline semiconductors with intrinsically low κ_l are highly sought after in TEs and other thermal energy management devices.

In pursuit of finding new low κ_l materials, different classes of crystalline compounds like the perovskites[20], half-Heuslers[21], full-Heuslers[22], and double half-Heuslers[11] have been explored using HT computational methods, and subsequently, some of the predicted compounds were experimentally synthesized successfully[9–11]. Despite the existence of a large number of crystalline compounds in various materials databases, e.g., the Inorganic Crystal Structure Database (ICSD)[23], Open Quantum Materials Database (OQMD)[3,4], Materials Project[5], and Aflowlib[24], it is quite important to look for hitherto unknown stable and metastable compounds which might exhibit exciting physical and chemical properties. In this work, we present the computational discovery of a large number of stable (628) and low-energy metastable (852) quaternary chalcogenides AMM′Q_3 (A = alkali, alkaline earth, post-transition metals; M/M′ = transition metals, lanthanides; Q = chalcogens) that span a huge chemical space across the periodic table. Our results are based on reliable, accurate, and robust HT-DFT calculations where (1) we generated initial AMM′Q_3 compositions following the experimentally known AMM′Q_3 compounds formation criteria, (2) calculated their energetics in all known seven crystallographic prototypes that are found in this materials family, and (3) performed thermodynamic phase stability analysis of these compositions against all possible competing phases that are present in the OQMD.

About 192 quaternary chalcogenides (see Supplementary Note for a complete list) with the generic formula AMM′Q_3 have been synthesized experimentally[25–33] which reveal that these compounds possess rich chemistries and structure types like the perovskites and Heusler compounds. Koscielski et al.[25] noted that these known AMM′Q_3 compounds contain no Q–Q bonds and the elements (A, M, M′, Q) balance the charge in their crystal structures with their expected formal oxidation states, making them charge balanced. The AMM′Q_3 compounds are further classified into three categories depending on the nominal oxidation states of the three cations A, M, and M′, namely:

---

[1]Department of Materials Science and Engineering, Northwestern University, Evanston, IL, USA. [2]Department of Chemistry, Northwestern University, Evanston, IL, USA. ✉email: koushik.pal.physics@gmail.com; c-wolverton@northwestern.edu

- Type-I ($A^{1+}M^{1+}M'^{4+}Q_3$)
- Type-II ($A^{2+}M^{1+}M'^{3+}Q_3$)
- Type-III ($A^{1+}M^{2+}M'^{3+}Q_3$),

where the oxidation states of the cations are indicated with the superscripts. In all cases, we assume that the chalcogen atoms Q (S, Se, and Te) have a nominal 2− charge. Examining the experimentally known $AMM'Q_3$ compounds (see Supplementary Fig. 1), we observe the following: (1) The A-site in these compounds is always occupied by alkali, alkaline earth, or post-transition metals with the only exception of Eu (in a 2+ charge state) which occupies the A-site of some of the Type-II compounds. (2) Whereas only transition metals occupy the M site, the M′ site can be filled either by the transition metals, lanthanides, or actinides. (3) No observed $AMM'Q_3$ compound contains more than one alkali, alkaline earth, or post-transition metals. As detailed later, we will use these criteria in designing our HT workflow for generating the initial crystal structures through prototype decoration. Although the crystal chemistries of these compounds have been characterized somewhat in detail[25–33], their properties have remained largely unexplored. Recently, it was shown experimentally[34] and theoretically[34–37] that many known semiconducting compounds in this crystal family exhibit ultralow κ_l. In addition, some compounds are shown to possess electronic bands favorable to support high TE performance[34,36,37].

From the distribution of the elements forming the known $AMM'Q_3$ compounds, we see that all the cations (A, M, M′) are in their common oxidation states of 1+, 2+, 3+, or 4+ coming from the chemical groups (i.e., alkali, alkaline earth, transition, post-transition metals, lanthanides, actinides) that span a large part of the periodic table. Yet, although a large number (192) of these compounds have been reported experimentally, this number is small compared to the vast number of possible compounds that can be obtained based on charge balanced combinatorial substitutions of the elements in a prototype crystal structure of $AMM'Q_3$. Performing this combinatorial exercise experimentally would require a massive amount of resources and time to discover new $AMM'Q_3$ compounds. However, computational screening can be very helpful in narrowing down the search space of the target compounds that would have higher chances of synthesizability in the laboratory[1,8–11,38–43]. Here, we have performed HT-DFT calculations followed by accurate ground-state phase stability analysis, and suggest ($T = 0$ K) thermodynamically stable and metastable $AMM'Q_3$ compounds for experimental synthesis and exploration of their properties. Our calculations of the thermal transport properties of some of the predicted stable compounds using the Peierls–Boltzmann transport equation (PBTE) show that these compounds exhibit innate low κ_l due to the presence of strong lattice anharmonicity or rattler cations.

RESULTS

Structural prototypes

The experimentally known $AMM'Q_3$ compounds crystallize in seven structure types[25–33]: $KCuZrSe_3$ (space group (SG): Cmcm, #63), Eu_2CuS_3 (SG: Pnma, #62), $BaCuLaS_3$ (SG: Pnma, #62), Ba_2MnS_3 (SG: Pnma, #62), $NaCuTiS_3$ (SG: Pnma, #62), $BaAgErS_3$ (SG: C2/m, #12), and $TlCuTiTe_3$ (SG: $P2_1/m$, #11). All these structure types are visualized in their extended unit cells in Fig. 1, where the conventional unit cell is outlined with black lines. Among these, five structure types ($KCuZrSe_3$, Eu_2CuS_3, Ba_2MnS_3, $NaCuTiS_3$, $TlCuTiTe_3$) are layered where the rows of A^{m+} cations stack alternatively with the $[MM'Q_3]^{m-}$ layers and interact through electrostatic interactions[35,37]. The strength of the interactions vary with the charges on the cations (i.e., m+) and induce modifications in the structures as well as in their properties[36]. When the interactions between the layers increase significantly, the atoms from the neighboring $[MM'Q_3]^{m-}$ layers interact, giving rise to the three-dimensional channel structures ($BaCuLaS_3$ and $BaAgErS_3$). In $BaCuLaS_3$ (Fig. 1c) and $BaAgErS_3$ (Fig. 1f), two rows of the A-site cations occupy the empty spaces inside the channels formed by the M, M′, and Q atoms. Figure 1h shows that 71% of the known $AMM'Q_3$ compounds crystallize in the $KCuZrSe_3$ structure followed by 16% of the compounds crystallizing in the Eu_2CuS_3 structure type. The rest of the known $AMM'Q_3$ compounds (13%) crystallize in the other five structure types. It is worth noting that in Eu_2CuS_3, the Eu atoms have mixed oxidation states ($Eu^{2+}CuEu^{3+}S_3$) and sit in two different sites in the crystal structure. Similarly, the Ba atoms in Ba_2MnS_3 also occupy two different sites. We have used all these structure types in our HT-DFT design and discovery of new $AMM'Q_3$ compounds. We note that the KCuZrSe3 and $TlCuTiTe_3$ structure types have 12 atoms in their primitive unit cells and the rest of the structure types have 24 atoms.

Materials design strategy

The discovery of new compounds through HT-DFT method often starts with the decoration of prototype crystal structures with chemically similar elements from the periodic table to generate their initial crystal structures. DFT calculations are then performed on these newly decorated compounds followed by rigorous thermodynamic phase stability analysis to screen for stable and metastable compounds. Rather than generating the input crystal structures in a brute-force manner by substituting every element of the periodic table at all atomic sites in the prototype structures, in this work we restricted ourselves by the following screening criteria which are derived by examining the experimentally known $AMM'Q_3$ compounds: (1) we substitute alkali, alkaline earth, or post-transition metal elements at the A-site. The M and M′ sites are populated with the transition metals and lanthanides. Three chalcogens, i.e., S, Se, and Te are substituted at the Q site. (2) We choose A-site cations with nominal oxidation states of 1+ or 2+, and M/M′-site cations with nominal oxidation states of 1+, 2+, 3+, or 4+. The elements that are chosen for substitutions at the A, M, M′ and Q sites along with their oxidation states are shown in Fig. 2. (3) We only consider compound compositions that are charge balanced. (4) We exclude any radioactive elements during the prototype decorations although some of the known $AMM'Q_3$ compounds contain them. Adhering to these preconditions helps us narrow down our search space of compound exploration, reduces the computational cost, and most importantly it increases the success rates of stable compound prediction through HT-DFT calculations which will be evident later.

First, we generate the crystal structures of 4659 $AMM'Q_3$ compositions (see Table 1) using the $KCuZrSe_3$ structure as (1) it is the most prevalent structure type in this family and (2) all experimentally known $AMM'Q_3$ compounds have low energies (within 50 meV/atom above the convex hull) in this structure type. After performing DFT calculations for all these compositions followed by $T = 0$ K phase stability analysis, we kept only those compounds (~1700) that have an energy within 50 meV/atom of the ground-state convex hull and discarded the rest from our search space. The DFT relaxed structures of all these 1700 compounds retain the $KCuZrSe_3$ structure type. In the next step, we take these 1700 compositions and regenerate their crystal structures in each of six additional structure types to perform DFT calculations of $6 \times 1700 = 10,200$ $AMM'Q_3$ compounds. Next, we perform $T = 0$ K thermodynamic phase stability analysis of those 1700 compositions considering all seven structure types and their competing phases that are available in the OQMD. In the final step, we obtain 628 thermodynamically stable and 852 metastable hitherto unknown $AMM'Q_3$ compounds after performing a total number of $4659 + 10,200 = 14,859$ DFT calculations. The stable 628 compounds include 69 Type-I, 231 Type-II, and 328 Type-III compounds, and among them, a total number of 570 compounds

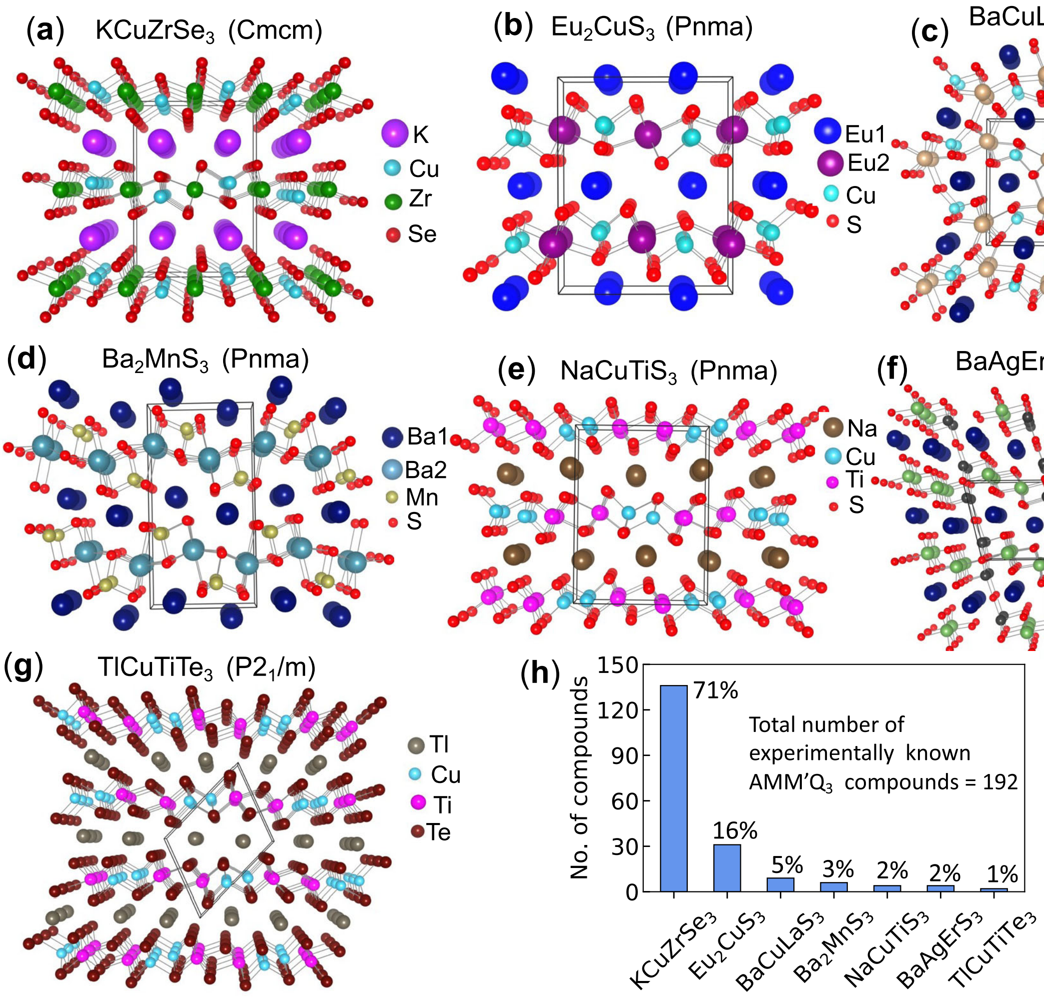

Fig. 1 Crystallographic prototypes of the AMM′Q$_3$ compounds. a–g Seven structural prototypes in the family of experimentally known AMM′Q$_3$ compounds. Most of them have layered crystal structures where the layers of A^{m+} cations are sandwiched between the covalently bonded layers of [MM′Q$_3$]$^{m-}$ anion sublattice, and interact with the later through electrostatic interactions. The black solid lines in each figure indicate the conventional unit cell of each compound. **h** Distributions of the experimentally known AMM′Q$_3$ compounds in the seven structure types.

possess finite band gaps. A schematic of the HT-DFT flowchart is shown in Fig. 3a, and a summary is given in Table 1.

Phase stability analysis

We now present a detailed analysis of the T = 0 K ground-state phase stability of all (known and predicted) AMM′Q$_3$ compounds. We begin our assessment with the phase stability analysis of the experimentally known AMM′Q$_3$. Out of 192 known compounds, we find only 119 compounds (Type-I: 39, Type-II: 30, and Type-III: 50) in OQMD before we performed any new calculations from this work. We designate these 119 compounds as Set-I. As the initial crystal structures of the experimentally known compounds in OQMD mostly come from the ICSD, the DFT calculations of Set-I compounds in OQMD were performed based on their experimental crystal structures taken from the ICSD. We designate the rest of the known 192 − 119 = 73 compounds (Type-I: 1, Type-II: 60, and Type-III: 12) as Set-II, which were not present in OQMD due to (1) the absence of their structures in the ICSD and (2) no previous HT-DFT calculations were performed based on the prototype decorations in this AMM′Q$_3$ family. However, our HT-DFT calculations of all the decorated AMM′Q$_3$ compositions include the experimentally known AMM′Q$_3$ compounds in Set-II. Hence, we will first analyze the phase stability of the Set-I compounds to see if our DFT calculations are able to correctly capture the energetics of the known compounds in Set-I and then we will utilize the phase stability data of Set-II compounds to validate the reliability of our approach for the discovery of new stable AMM′Q$_3$ compounds based on prototype decoration through HT-DFT calculations.

As detailed in the "Methods" section and as well as in other references[1,3–6,24,41,44], the hull distance (hd) is a metric of the thermodynamic stability of a compound. If the formation energy of the compound breaks the convex hull, then it is considered to be thermodynamically stable with hd = 0, indicating the likelihood of its synthesizability. On the other hand, compounds with a small positive hd (typically within a few tens of meV/atom) are called metastable and may also be in some cases experimentally synthesized[39,40]. According to these criteria, all experimentally known AMM′Q$_3$ compounds should possess zero or small positive hd's. Our analysis reveals that in Set-I, all (39) Type-I compounds and all but one (29) Type-II compounds have hd = 0, which is in line with our expectations. The one Type-II compound that has a small positive hd is Eu^{2+}CuEu^{3}+S$_3$ (hd = 37 meV/atom). Also, all but three (47) Type-III compounds of Set-I have hd = 0. These three Type-III compounds are CsCoYbS$_3$ (hd = 192 meV/atom), CsCoYbSe3 (hd = 151 meV/atom), CsZnYbSe$_3$ (hd = 76 meV/atom). So, 115 of 119 experimentally synthesized compounds in

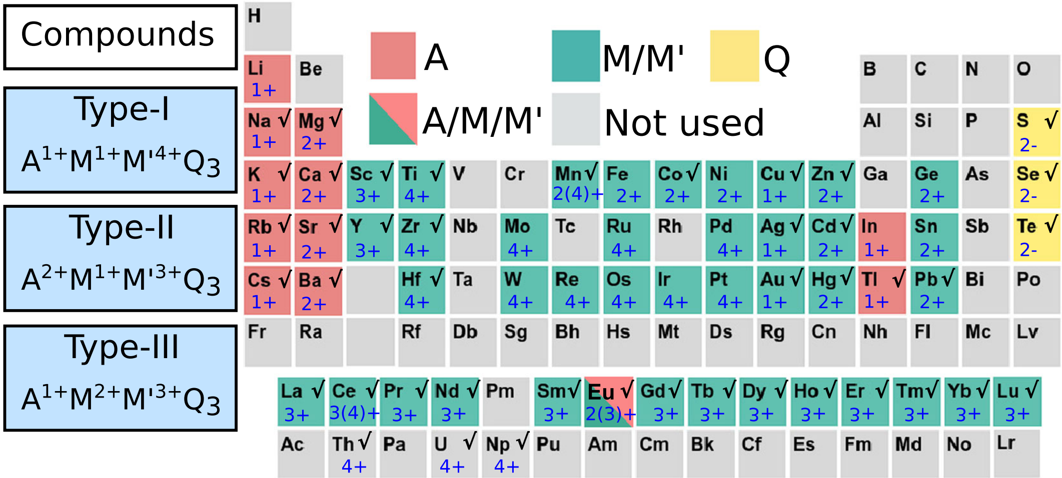

Fig. 2 Elemental distributions of the experimentally known and theoretically decorated AMM′Q_3 compounds. The AMM′Q_3 compounds are categorized into three types depending on the nominal oxidation states of the cations: Type-I ($A^{1+}M^{1+}M'^{4+}Q_3$), Type-II ($A^{2+}M^{1+}M'^{3+}Q_3$), and Type-III ($A^{1+}M^{2+}M'^{3+}Q_3$). The color-coded periodic table indicates the group of elements (whose oxidation states are written in blue color) that are used for prototype decorations in our HT-DFT calculations. Elements that are denoted with the check marks constitute the experimentally known AMM′Q_3 compounds. Salmon, cyan, and yellow colors represent elements that occupy A, M/M′, and Q sites, respectively. The gray color represents the elements that were not used for prototype decoration. Eu has mixed oxidation states and occupies both A and M′ site. Although Ba occupies A/M′ sites in Ba_2MnS_3, we have kept Ba fixed only to the A-site in this work during prototype decoration. All experimental and decorated compounds are charge balanced.

Table 1. A table summarizing the design and discovery of materials through prototype decoration.

	Type-I	Type-II	Type-III	Total
A	Li, Na, K, Rb, Cs, In, Tl (7)	Mg, Ca, Sr, Ba, Ge, Sn, Pb, Eu (8)	Li, Na, K, Rb, Cs, In, Tl (7)	–
M	Cu, Ag, Au (3)	Cu, Ag, Au (3)	Mn, Fe, Co, Ni, Zn, Cd, Hg, Eu (8)	–
M′	Ti, Mn, Zr, Mo, Ru, Pd, Hf, W, Re, Os, Ir, Pt, Ce (13)	Sc, Y, La, Ce, Pr, Nd, Sm, Eu Gd, Tb, Dy, Ho, Er, Tm, Yb, Lu (16)	Sc, Y, La, Ce, Pr, Nd, Sm, Eu Gd, Tb, Dy, Ho, Er, Tm, Yb, Lu (16)	–
Q	S, Se, Te (3)	S, Se, Te (3)	S, Se, Te (3)	–
Total number of initial compositions	$7\times3\times13\times3=819$	$8\times3\times16\times3=1152$	$7\times8\times16\times3=2688$	4659
Thermodynamically stable compounds	69	231	328	628
Thermodynamically metastable compounds	59	282	511	852

Elements chosen for decorating the prototype AMM′Q_3 structures and results of HT-DFT calculations are shown here. The values within the parentheses indicate the total number of elements used in each of three categories of compounds for substitutions at the A, M, M′, and Q sites. All generated initial compositions satisfy the charge neutrality criteria based on their nominal oxidation states. The numbers of predicted stable (hd = 0) and low-energy metastable ($0 < \text{hd} \leq 50$ meV/atom) compounds in the table exclude the experimentally known 192 AMM′Q_3 compounds.

Set-I are thermodynamically stable in the OQMD. Hence, stability is an excellent metric for the synthesizability of the predicted compounds. From this analysis, we also find that one of the Type-II compounds in Set-I, $BaAgErS_3$, possesses a small positive hd of 12 meV/atom when its calculation is performed on the experimental crystal structure having C2/m SG (#12), indicating that it is metastable at 0 K in this structure. Interestingly, our HT-DFT calculations reveal that $BaAgErS_3$ is stable T = 0 K in the $KCuZrSe_3$ structure type (see Supplementary Fig. 2).

Since the 73 compounds in Set-II did not exist in OQMD before our HT-DFT calculations, we generate their crystal structures through prototype decorations as mentioned before to perform DFT calculations and T = 0 K phase stability analysis. As these compounds have already been synthesized experimentally, our DFT calculations and phase stability analysis provide a key test of our methodology. It also gives us an opportunity to examine how reliably our calculations can predict hitherto unknown stable AMM′Q_3 compounds. After performing the thermodynamic stability analysis, we found that among the 73 compounds in Set-II (type-I: 1, type-II: 60, type-III: 12), 64 compounds have hd = 0, and only four compounds (SrCuYbS3: hd = 84 meV/atom, $BaCuYbTe_3$: hd = 62 meV/atom, $EuCuYbS_3$: hd = 72 meV/atom, $PbCuYbS_3$: hd = 104 meV/atom) of Type-II and five compounds ($CsMnYbSe_3$: hd = 8 meV/atom, $CsZnYbS_3$: hd = 163 meV/atom, $CsZnYbTe_3$: hd = 71 meV/atom, $RbZnYbSe_3$: hd = 102 meV/atom, $RbZnYbTe_3$: hd = 82 meV/atom) of Type-III have positive hd's.

Thus, our HT-DFT calculations based on the decorated structures successfully capture the stability of all but 13 (out of 192) of the experimentally known AMM′Q_3 compounds. The 13 compounds which are experimentally observed but with hd > 0 all contain Eu and Yb, and the calculated energetics of these compounds may originate from the choice of incorrect pseudopotentials as discussed later. These results and analysis give us strong confidence in designing and discovering new AMM′Q_3 compounds using the HT-DFT calculations and thermodynamic T = 0 K stability as a metric for synthesizable compounds. We have

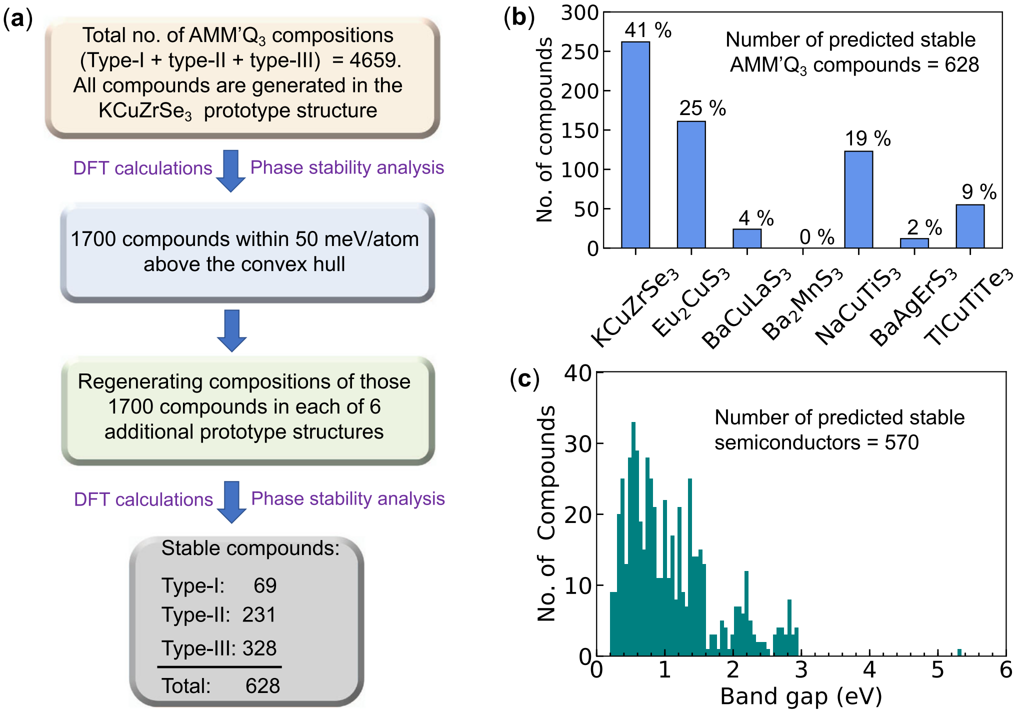

Fig. 3 A brief workflow and summary of high-throughput DFT calculations. a A schematic flowchart of the HT-DFT calculations for the discovery of new AMM′Q_3 compounds. **b** The distribution of 628 predicted stable compounds in the seven structure types. **c** 570 out of 628 compounds possess finite band gaps. Histogram plot for the DFT-calculated band gaps of these 570 semiconductors.

provided the phase stability data of all 192 experimentally known AMM′Q_3 compounds in the Supplementary information.

Discovery of AMM′Q_3 compounds

After performing the $T = 0$ K stability analysis of all newly decorated AMM′Q_3 compounds for which HT-DFT calculations are performed in all seven structure types, we discover a large number of 628 (type-I: 69, type-II: 231, type-III:328) thermodynamically stable compounds that exclude the experimentally known 192 compounds. To put this number into perspective, the OQMD (containing more than 900,000 entries as of September 2020) has stable (hd = 0) 1161 full-Heuslers (SG: $Fm\bar{3}m$, #225), 618 half-Heuslers (SG: $F\bar{4}3m$, #216), 353 cubic (SG: $Pm\bar{3}m$, #221) perovskites, 242 orthorhombic (SG: Pnma, #62) perovskites. Similar to the experimentally known AMM′Q_3 compounds, the $KCuZrSe_3$ and Eu_2CuS_3 structure types are the most common, which constitute 41% and 25% of the predicted stable compounds, respectively (Fig. 3b). Among the other structure types, $NaCuTiSe_3$ and $TlCuTiTe_3$ are quite common, which constitute 19% and 9% of the predicted stable compounds. The rest 6% compounds have the $BaCuLaS_3$ and $BaAgErS_3$ structure types. However, we found no new stable compound in the Ba_2MnS_3 structure type. Our analysis shows that 570 out of 628 compounds possess finite bands that range from 0.2 to 5.34 eV, among which most of the compounds have band gaps within 1.5 eV (Fig. 3c). This is not surprising since all the decorated compositions are charge balanced. In addition, we found 852 potentially synthesizable metastable compounds (Type-I: 59, Type-II: 282, Type-III: 511) with small positive hds (i.e., $0 < hd \leq 50$ meV/atom). A summary of the HT-DFT calculations is shown in Table 1, and the lists of all predicted stable and metastable compounds are given in the Supplementary information.

We further examine the predicted stable compounds within each type in terms of their chemistries (sulfides, selenides, and tellurides) and the cations (A, M, M′). The results are displayed as bar charts in Fig. 4, where the bar corresponding to an element represents the number of stable compounds that contain it. We see that: (1) the elements that form the stable compounds constitute almost the entire periodic table. (2) There are more Cu-containing compounds in Type-I and Type-II categories compared to Ag or Au. In Type-III, there are more Mn compounds than other M elements with a 2+ oxidation state. (3) The number of stable compounds increases from Type-I (69) to Type-II (231) to Type-III (328). This is not surprising given that the number of elements that can occupy the M and M′ sites (satisfying the charge neutrality criteria) increase from Type-I to Type-III compounds (Table 1). A general trend that is noticeable across three types is that as we go from sulfides to selenides to tellurides, the number of compounds with smaller A cations decrease whereas the number increases with larger A cations. For example, there are two, two, and no Li-containing compounds in sulfides, selenides, and tellurides of Type-I compounds, respectively. Similarly, the number of compounds that have Sr increase from sulfides (7) to selenides (20) to tellurides (34) in Type-II.

Lattice thermal transport properties

We now focus on exploring the lattice thermal transport properties of the predicted stable AMM′Q_3 compounds. An accurate estimation of κ_l of a compound within a first-principles DFT framework is computationally very expensive[45]. Hence, the calculations of κ_l for all the predicted stable compounds would require a massive amount of computational resources. However, to demonstrate the thermal transport properties of our newly predicted stable compounds, we randomly select a handful of compounds with some criteria. We first screen for non-magnetic and semiconducting compounds, where the lattice contribution dominates the total thermal conductivity. Next, we search for those compounds which have the $KCuZrSe_3$ structure type as it possesses the highest crystal symmetry (SG: Cmcm, #63) and the smallest unit cell (12 atoms). Finally, we randomly select ten compounds for κ_l calculations. The selected compounds, which include sulfides, selenides, and tellurides, are: $CsCuZrS_3$,

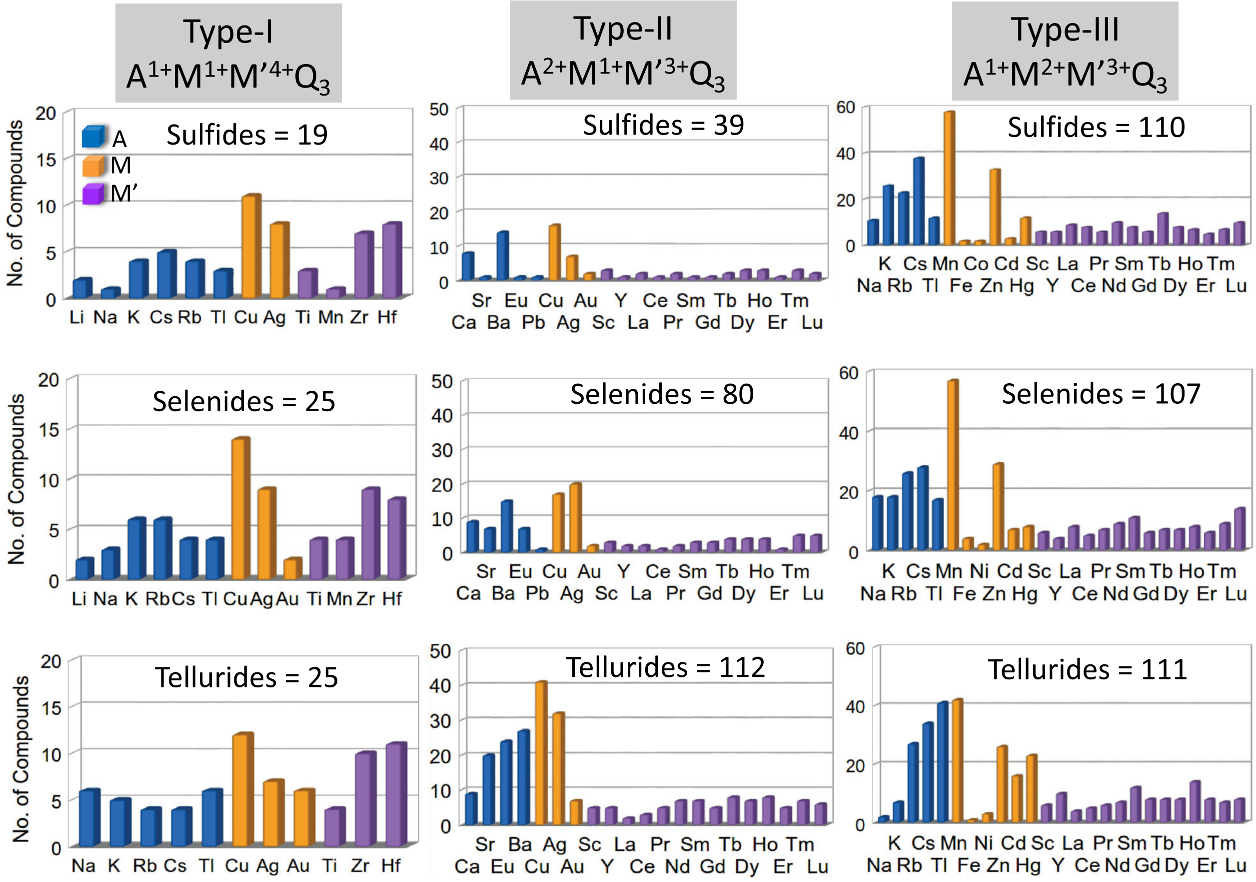

Fig. 4 Elemental distributions of the predicted stable AMM′Q_3 compounds. Distributions of the cations (A, M, M′) forming the 628 predicted stable AMM′Q_3 compounds in the three categories: Type-I, Type-II, and Type-III. The bar corresponding to an element represents the number of stable compounds containing it. Total number of sulfides, selenides, and tellurides are mentioned in each panel. These compounds exclude the experimentally known 192 AMM′Q_3 compounds.

$BaCuScSe_3$, $BaCuScTe_3$, $BaCuTbSe_3$, $BaAgGdSe_3$, $CsZnYS_3$, $CsZnGdS_3$, $CsZnScSe_3$, $CsZnScTe_3$, $CsCdYTe_3$. We note that this list also includes Type-I (the first in the list), Type-II (the next 4) as well as Type-III (the last 5) compounds. The electronic structures and phonon dispersions of these compounds are given in the Supplementary information.

We calculate the κ_l of these ten compounds using the PBTE (see "Methods" section) and present the results in Fig. 5. We see that all these compounds exhibit very low κ_l where the in-plane ($\kappa_l^{\perp}$) and the cross-plane ($\kappa_l^{\parallel}$) components are lower than 3 $Wm^{-1}K^{-1}$ and 1.2 $Wm^{-1}K^{-1}$, respectively, for $T \geq 300$ K. Here, $\kappa_l^{\perp}$ is perpendicular to the stacking direction of the layers in the crystal structure of the AMM′Q_3 compounds and $\kappa_l^{\parallel}$ is parallel to it. As a reference, we compare our calculated κ_l with that of a prototypical TE material SnSe, which was experimentally shown to possesses low κ_l that leads to a very high TE figure-of-merit[46]. The measured[47] $\kappa_l^{\perp}$ and $\kappa_l^{\parallel}$ for single-crystalline stoichiometric samples of SnSe are 1.9 and 0.9 $Wm^{-1}K^{-1}$, respectively, at 300 K, which become much lower in the off-stoichiometric polycrystalline samples[46]. Further examination of the results in Fig. 5 reveals that in terms of the anisotropy of the $\kappa_l^{\perp}$ and $\kappa_l^{\parallel}$ components, Type-I and Type-III compounds are quite similar, but Type-II compounds are different from the rest i.e., $\kappa_l^{\perp}/\kappa_l^{\parallel}$ (Type-I/III) > $\kappa_l^{\perp}/\kappa_l^{\parallel}$ (Type-II). The difference in the anisotropy of the properties arises from the fact that in Type-II compound the electrostatic attractions between A^{2+} and $[MM'Q_3]^{2-}$ layers are stronger than that of between A^{1+} and $[MM'Q_3]^{1-}$ layers in Type-I/III compounds. The stronger interlayer interactions give rise to a shorter interlayer distance in Type-II, which make $\kappa_l^{\perp}$ and $\kappa_l^{\parallel}$ less anisotropic.

To gain a deeper understanding, we examine the lattice dynamics and thermal transport properties of $BaCuScTe_3$ (Type-II) and $CsCdYTe_3$ (Type-III) in detail. Our analysis reveals that the underlying physical principles governing the low κ_l in Type-II compounds are different from the Type-I/III compounds. We start our analysis with the phonon dispersion of $BaCuScTe_3$ (Fig. 6a), which shows the presence of very low-frequency acoustic (<45 cm^{-1}), and optical (~15 cm^{-1} along X-S-R directions) phonon modes, which give rise to low phonon group velocities. The phonon dispersion and the phonon density of states (Fig. 6b) of $BaScCuTe_3$ show that a strong hybridization exists between the phonon branches up to 100 cm^{-1}, where Ba and Te atoms have large contributions. Soft acoustic phonon branches give rise to very low-sound velocities and a strong hybridization between the phonons at low energies enhances the phonon scattering phase space. Both these factors help suitably to give rise to a very low κ_l ($\kappa_l^{\perp} = 1.7$ $Wm^{-1}K^{-1}$ and $\kappa_l^{\parallel} = 0.76$ $Wm^{-1}K^{-1}$ at 300 K). On the other hand, the phonon dispersion of $CsCdYTe_3$ (Fig. 6d) features nearly dispersion-less optical phonon branches along the X-S-R-A directions in the Brillouin zone at low energies, which are the characteristics of rattler vibrations in the crystal structure. In addition, it also has soft acoustic phonon branches (<35 cm^{-1}). The calculated κ_l of $CsCdYTe_3$ becomes ultralow with $\kappa_l^{\perp}$ and $\kappa_l^{\parallel}$ being 0.82 and 0.25 $Wm^{-1}K^{-1}$, respectively, at 300 K.

Rattler phonon modes are highly localized, which strongly inhibit the transport of phonons, giving rise to ultralow κ_l in many crystalline solids such as $TlInTe_2$[48], $CsAg_5Te_3$[49], etc. It was shown that the filler atoms in clathrates[50] and skutterudites[51] act as ideal rattlers, which give rise to dispersion-less phonon branches where

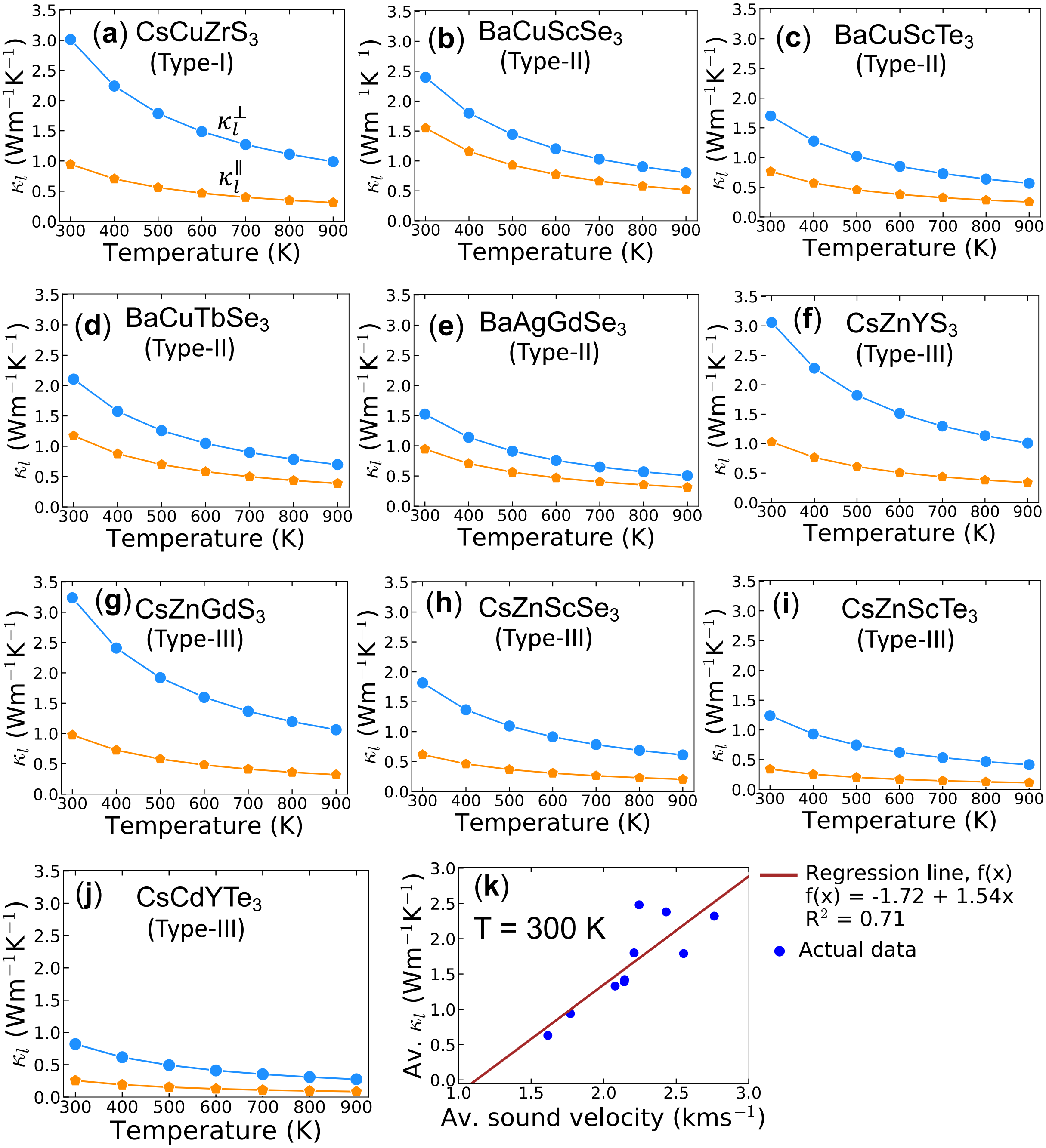

Fig. 5 Lattice thermal transport properties of the AMM′Q$_3$ compounds. a–j The calculated temperature-dependent lattice thermal conductivity (κ_l) of ten predicted stable AMM′Q$_3$ compound which are non-magnetic and semiconducting. $\kappa_l^\perp$ (blue disk) and $\kappa_l^\parallel$ (orange pentagon) are the two components of κ_l that are perpendicular and parallel to the stacking directions in the crystal structure, respectively. **k** Predictive statistical model of κ_l. A linear regression model, *f*(*x*), is fitted to the average (Av.) sound velocity vs average κ_l data (at 300 K) of those ten compounds, which is used to predict κ_l of other AMM′Q$_3$ compounds based on their average speed of sounds.

the phonon frequencies remain highly localized having very small participation ratio (PR) values ~0.2 (see "Methods" section). The PRs of the phonon modes of BaCuScTe$_3$ and CsCdYTe$_3$ are color coded in Fig. 6a, d, respectively. We see that while most of the low-energy phonon modes (<100 cm^{-1}) of BaCuScTe$_3$ have PR values close to 1, signifying the absence of phonon localization, the low-energy dispersion-less phonon branches of CsCdYTe$_3$ have small PRs (<0.2), indicating the highly localized nature of the phonon modes. The phonon density of states (Fig. 6e) also reveals that these localized phonons primarily arise from the Cs atoms (confined in 25–55 cm^{-1}) that act as rattlers. Thus, our analysis shows that the ultralow κ_l in CsCdYTe$_3$ is primarily caused by the localized vibrations of the rattling phonons.

We further investigate the origin of such poor thermal transport properties in BaCuScTe$_3$ in terms of a more fundamental material quantity, the lattice anharmonicity. Strong lattice anharmonicity is one of the important factors that induces very low κ_l in compounds like SnSe[52], NaSbTe$_2$[53], etc. To estimate the strength

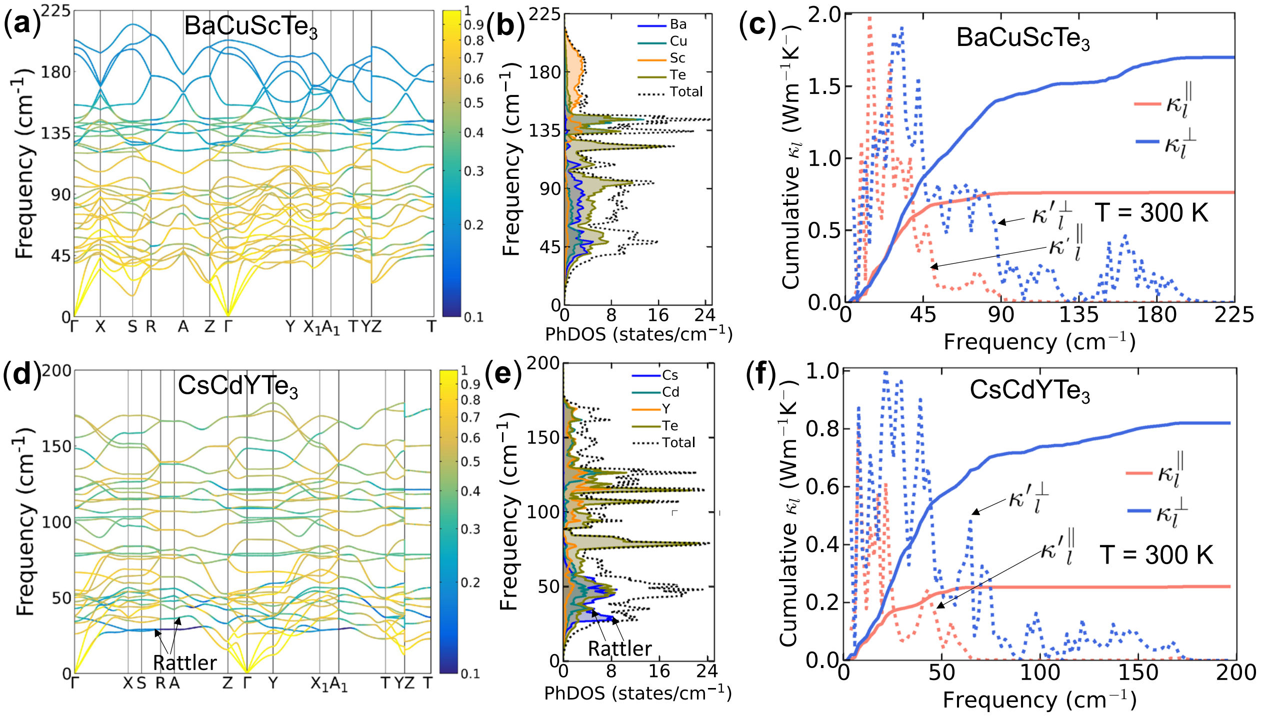

Fig. 6 Harmonic and anharmonic lattice dynamical properties of the AMM′Q$_3$ compounds. Harmonic phonon dispersions, atom-resolved phonon density of states, anharmaonic frequency-cumulative κ_l, and their derivatives with respect to the frequency for BaCuScTe$_3$ (**a**–**c**) and CsCdYTe$_3$ (**d**–**f**). The phonon dispersions are color coded with the participation ratios of the phonon modes (indicated in the color bar). $\kappa_l^{\perp}$ (solid blue line) and $\kappa_l^{\parallel}$ (solid red line) are perpendicular and parallel to the stacking directions in the crystal structure of the AMM′Q$_3$ compound, respectively. $\kappa_l'^{\perp}$ (dotted blue line) and $\kappa_l'^{\parallel}$ (dotted red line) are the first-order derivatives of $\kappa_l^{\perp}$ and $\kappa_l^{\parallel}$, respectively, with respect to the frequency, which are in arbitrary units in the figures.

of the intrinsic anharmonicity, we calculate the macroscopic average Gruneisen parameter,

$$\gamma = \sum_i \gamma_i C_{\mathrm{v,i}} / \sum_i C_{\mathrm{v,i}}, \qquad (2)$$

where γ_i and $C_{\mathrm{v,i}}$ are the Gruneisen parameter and specific heat capacity at constant volume for the ith phonon mode. The calculated γ of BaCuScTe$_3$ (1.5) is larger than that of CsCdYTe$_3$ (1.2), signifying the presence of stronger anharmonicity in the former. These γ values are comparable to that of NaSbSe$_2$ (1.7), NaSbTe$_2$ (1.6), NaBiTe$_2$ (1.5), etc. compounds which are experimentally[53] shown to possess ultralow κ_l. Thus, we see that while the low κ_l in Type-II compounds is caused by the low-sound velocities and a stronger lattice anharmonicity, the presence of rattler cations in Type-III as well Type-I compounds (see Supplementary Fig. 4) are primarily responsible for inducing low κ_l in them.

To examine which phonons are primarily responsible for the conduction of heat in BaCuScTe$_3$ and CsCdYTe$_3$, we plot the cumulative-κ_l and their first-order derivatives (κ_l') with respect to the frequency at T = 300 K. We see from Fig. 6c that while the acoustic and low-energy optical phonons up to 90 cm^{-1} mainly contribute to $\kappa_l^{\perp}$, $\kappa_l^{\parallel}$ is primarily contributed by the phonons up to 45 cm^{-1} in BaCuScTe$_3$. On the other hand, Fig. 6f shows that while the acoustic as well as the optical phonons up to 100 cm^{-1} have large contributions toward $\kappa_l^{\perp}$, only the acoustic phonons (up to 35 cm^{-1}) primarily carry heat for $\kappa_l^{\parallel}$ in CsCdYTe$_3$. We also notice that the anisotropy ($\kappa_l^{\perp}/\kappa_l^{\parallel} = 3.3$ at T = 300 K) in CsCdYTe$_3$ is much larger that of BaCuScTe$_3$ ($\kappa_l^{\perp}/\kappa_l^{\parallel} = 2.2$ at T = 300 K). The origin of this anisotropy can be attributed to the contrasting interlayer and intralayer interactions in BaCuScTe$_3$ and CsCdYTe$_3$. For example, the analysis of the interatomic force constants (IFCs) reveals that interlayer interactions in CsCdYTe$_3$ are much weaker (IFC$_{\mathrm{(Cs-Te)}} = -0.333$ eV/Å^2) compared to BaCuScTe$_3$ (IFC$_{\mathrm{(Ba-Te)}} = -1.204$ eV/Å^2), which makes the transport of optical phonons (above 25 cm^{-1}) along the stacking direction (i.e., $\kappa_l^{\parallel}$) of CsCdYTe$_3$ less effective. On the other hand, the intralayer interactions in CsCdYTe$_3$ are much stronger (IFC$_{\mathrm{(Cd-Te)}} = -3.923$ eV/Å^2, IFC$_{\mathrm{(Y-Te)}}$: -2.216 eV/Å^2) than those of BaCuScTe$_3$ (IFC$_{\mathrm{(Cu-Te)}} = -2.396$ eV/Å^2, IFC$_{\mathrm{(Sc-Te)}} = -1.890$ eV/Å^2). As a result, while phonons up to 90 cm^{-1} mainly carry the heat for $\kappa_l^{\perp}$ in BaCuScTe$_3$, in CsCdYTe$_3$ they are carried by phonons with frequencies up to 100 cm^{-1} very effectively.

DISCUSSION

We notice that in Set-I and Set-II, all the known compounds that have positive hd's have either Yb^{3+} or Eu^{3+} cations in them. Given the fact OQMD used Yb_2 and Eu_2 PPs which are intended for compounds having Yb^{2+} and Eu^{2+} cations, those energetic results are somewhat suspect. However, we note that our HT-DFT calculations predict the stability of other rare-earth elements containing known compounds in this family correctly. Hence, the newly predicted compounds containing Eu^{3+} and Yb^{3+} should be taken with caution. We note that none of our predicted stable compounds contain these cations. However, 11 and 7 of the predicted metastable compounds contain Eu^{3+} and Yb^{3+} cations, respectively.

Concerning the experimental validation of our prediction, we note that the experimental synthesis of a large number of compounds is a daunting task. While automated synthesis of a large number of compounds is now possible through HT experimental facilities[54], here, we suggest only four compounds (Table 2) that can be immediately picked up for experimental verification of our prediction. These compounds contain no toxic element and their calculated lattice thermal conductivity is very

Table 2. Suggested compounds for experimental synthesis and characterization.

Compound	Band gap (eV)	Average γ at 300 K	Average κ_l ($\mathrm{Wm^{-1}\,K^{-1}}$) at 300 K	$\lvert S\rvert$ ($\mu\mathrm{VK^{-1}}$) at 600 K	PF ($\mu\mathrm{W\,cm^{-1}\,K^{-2}}$) at 600 K	ZT at 600 K	Direction/doping
$BaCuScTe_3$	0.39	1.51	1.23	254	11	0.63	In-plane/n-type
$BaAgGdSe_3$	1.45	1.60	1.24	260	14	1.1	Out-of-plane/p-type
$CsZnScTe_3$	1.20	1.30	0.79	400	25	1.3	Out-of-plane/p-type
$CsCdYTe_3$	1.74	1.30	0.54	390	13	1.4	In-plane/n-type

A list of four predicted stable compounds is suggested for the experimental synthesis and measurement of their properties. The DFT-calculated band gap, macroscopic average Gruneisen parameter (γ), the average κ_l are provided to compare against experiments. To highlight the thermoelectric performance of these compounds, we provide the Seebeck coefficient (S), power factor (PF), and ZT of these compounds at 600 K and at a nominal carrier concentration ($2\times10^{19}\,\mathrm{cm^{-3}}$) for $\tau = 10$ fs along the crystallographic direction and doping type for which ZT exhibits the maximum value.

low. In Table 2, we provide their DFT-calculated band gaps, γ, and average κ_l calculated at 300 K. These calculated quantities along with κ_l can be compared with the experimentally measured values of these materials. Finally, we note that κ_l for each compound has been calculated using only three-phonon scattering processes. The inclusion of additional four-phonon scattering rates[55,56] and grain-boundary[57] limited phonon scattering mechanisms could further lower the calculated κ_l in this family of compounds. Also, as the electronic structure of the compounds features nearly flat bands and multiple peaks near the valence/conduction band extrema (Supplementary Fig. 3), some of these compounds are expected to exhibit good potential for TE applications as well.

To estimate the usefulness of these materials as TEs, we perform detailed TE calculations (see "Methods" section for details) on the four compounds in Table 2. Our analysis shows that ZT of three compounds ($BaAgGdSe_3$, $CsZnScTe_3$, and $CsCdYTe_3$) exceeds 1 at 600 K, indicating their high TE performance. To highlight the TE efficiency of these four compounds, in Table 2, we provide the Seebeck coefficient, power factor and ZT (at 600 K) at a nominal carrier concentration ($2\times10^{19}\,\mathrm{cm^{-3}}$). We provide detailed characterization of TE properties of these compounds in the Supplementary Information (Supplementary Discussion and Supplementary Figs. 5–8).

Finally, we comment on the general trend of κ_l on other predicted stable $AMM'Q_3$ compounds. To achieve this, we have made a predictive statistical model, $f(x)$, of κ_l using the linear regression technique (see Fig. 5k and "Methods" section for details) which can be used to predict κ_l of any $AMM'Q_3$ compound based on its average speed of sound and without explicitly doing PBTE calculations. To this end, we randomly choose ten compounds (predicted, stable) that are different from Fig. 5, and calculate their average speed of sounds using which we predict their average κ_l at 300 K. These compounds and their predicted κ_l are: $NaZnHoSe_3$ ($1.24\,\mathrm{Wm^{-1}\,K^{-1}}$), $BaCuTbTe_3$ ($1.17\,\mathrm{Wm^{-1}\,K^{-1}}$), $CsCuHfS_3$ ($2.20\,\mathrm{Wm^{-1}\,K^{-1}}$), $SrCuHoSe_3$ ($1.69\,\mathrm{Wm^{-1}\,K^{-1}}$), $BaAgPrTe_3$ ($1.25\,\mathrm{Wm^{-1}\,K^{-1}}$), $KCdTbS_3$ ($1.73\,\mathrm{Wm^{-1}\,K^{-1}}$), $NaZnGdSe_3$ ($2.02\,\mathrm{Wm^{-1}\,K^{-1}}$), $CsCdLaSe_3$ ($1.00\,\mathrm{Wm^{-1}\,K^{-1}}$), $RbZnYTe_3$ ($0.95\,\mathrm{Wm^{-1}\,K^{-1}}$), $RbCuZrSe_3$ ($1.82\,\mathrm{Wm^{-1}\,K^{-1}}$). From these results, we see that the predicted $AMM'Q_3$ compounds generically exhibit very low κ_l.

In summary, we use HT-DFT calculations to discover a large number of 628 thermodynamically stable quaternary chalcogenides ($AMM'Q_3$). As all compositions in this family are charge balanced, our analysis shows that 570 of 628 compounds possess finite band gaps which vary between 0.2 and 5.34 eV. Our calculations of the thermal transport properties show that $AMM'Q_3$ compounds exhibit intrinsically very low κ_l, and the anisotropy in κ_l is much smaller in Type-II compounds compared to Type-I/III compounds. Our analysis further reveals that low κ_l in this family originates either due to the presence of rattling cations (in Type-I/III compounds) or stronger lattice anharmonicity (Type-II compound). While the rattler cations give rise to localized phonon modes that inhibit the propagation of phonons, a stronger lattice anharmonicity enhances the phonon scattering phase space, leading to a low κ_l. In addition, there exists a strong coupling between the acoustic and low-energy optical phonon modes in Type-II compounds which increases the phonon scattering rates of the heat-carrying phonons. A detailed TE characterization of some of the predicted compounds show the potential of the $AMM'Q_3$ compounds to be efficient TEs. Our work is thus interesting not just from the perspective of materials discovery but also for finding the presence of low κ_l in them, which hold promises for further research and possible applications in energy materials, particularly in TEs and related devices.

METHODS

DFT calculations

We performed DFT calculations using the Vienna Ab initio Simulation Package[58] and utilizing the projector-augmented wave[59] potentials with the Perdew–Burke–Ernzerhof[60] generalized gradient approximation to the exchange-correlation functional. The atomic positions and other cell degrees of freedom of the compounds were fully relaxed and spin-polarized calculations were performed for compounds that contain partially filled d or f-shells elements with a ferromagnetic arrangement of spins in accordance with the HT framework as laid out in the qmpy suite of tools[3,4]. For more details on the calculation parameters, we refer to refs. [3,4]. T = 0 K phase stability analysis often serves as an excellent indicator for the possibility of synthesizability of a predicted compound in the laboratory[9–11]. To assess the T = 0 K thermodynamic stability of the compounds, we calculate their formation energies (ΔH_f) utilizing the DFT total energy (ground-state) of each compound using the formula:

$$\Delta H_f(\sigma) = E(\sigma) - \sum_i n_i \mu_i, \tag{3}$$

where E is the DFT total energy (at 0 K) of an $AMM'Q_3$ compound in a crystal structure denoted by σ, μ_i is the chemical potential of element i with its fraction n_i in that compound. For each composition, we used a number of prototype crystal structures, σ, based on structural prototypes of known $AMM'Q_3$ compounds. To determine the thermodynamic stability of a compound, we need to compare its formation energy against all its competing phases, not only against other compounds at the same composition. To this end, we generated the quaternary phase diagram (i.e., the T = 0 K convex hull of the A-M-M′-Q phase space) for every $AMM'Q_3$ compound considering all elemental, binary, ternary, and quaternary phases present in the OQMD, which (as of September 2020) corresponded to nearly 900,000 entries of DFT-calculated energies. The calculated convex hd (explained in the next section) then serves as a metric to determine whether a compound is stable (i.e., hd = 0), metastable (small positive hd), or unstable (large positive hd).

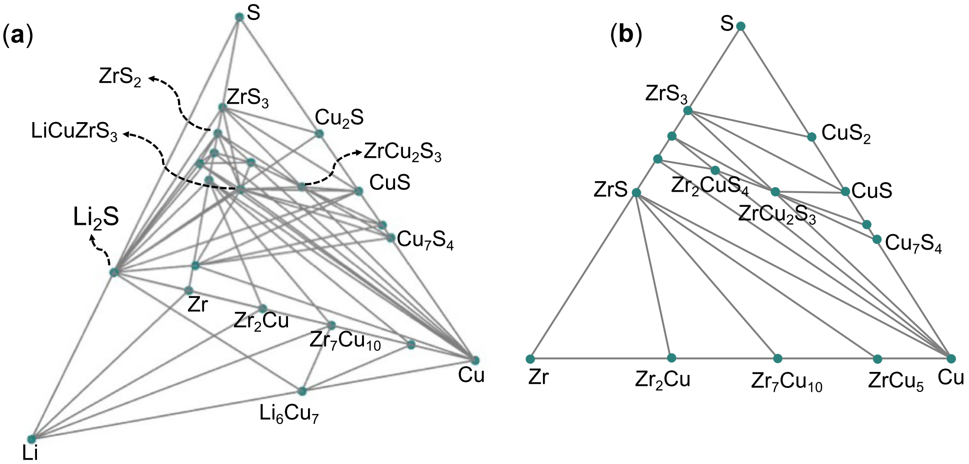

Fig. 7 Visualization of quaternary and ternary phase diagrams. a The four-dimensional phase diagram (T = 0 K) of the Li-Cu-Zr-S quaternary system, which is the isometric shot of a Gibbs' tetrahedron. **b** One of the faces of the tetrahedron represents the three-dimensional phase diagram of the Cu-Zr-S ternary system which is presented as the Gibbs' triangle. Each cyan node in **a** and **b** represents a stable compound. For clarity, we do not show any metastable/unstable compounds and mark only few stable compounds in this figure. $LiCuZrS_3$ is one of the predicted stable compounds in this work, which and its competing phases are denoted with dashed arrows in **a**.

Convex hull construction

To construct the convex hull of an $AMM'Q_3$ compound, it is necessary to identify the set of phases (elemental, binary, ternary as well as quaternary) in the four-dimensional composition space of A-M-M′-Q that have the lowest formation energies at their compositions. In OQMD, we present the convex hull of a quaternary compound through a four-dimensional phase diagram which is represented as an isometric shot of the Gibbs' tetrahedron (Fig. 7a). Each face of the tetrahedron represents a three-dimensional phase diagram of a ternary composition that is represented as the Gibbs' triangle (Fig. 7b). The vertices in Fig. 7a, b represent the elements constituting the quaternary and ternary phase space, respectively, and the edges connecting any two vertices represent the binary composition axis between those two elements. Any node within Fig. 7a, b represents a stable compound, which is denoted by a cyan disk. The metastable and unstable compounds are not shown in these figures for clarity which fall off the nodes. The stability of an $AMM'Q_3$ compound is given by the difference (which is defined as the hd) between the calculated formation energy (ΔH_f) of an $AMM'Q_3$ compound under consideration and its hull energy (ΔH_e) at that composition:

$$hd = \Delta H_f - \Delta H_e. \tag{4}$$

The hull energy is defined as the energy at the convex hull at that $AMM'Q_3$ composition. By definition, the hd of a stable compound is zero, whereas for metastable and unstable compounds they are real positive numbers. In keeping with the heuristic conventions used in literature[10,61,62] we term those $AMM'Q_3$ compounds to be metastable whose hd's lie within 50 meV/atom above the convex hull (i.e., $0 < hd \leq 50$ meV/atom). The metastable compounds are also potentially synthesizable in the laboratory[39,40].

Phonon participation ratio

Phonon dispersions have been calculated using $2 \times 2 \times 1$ supercell of the primitive unit cell using Phonopy[63]. The high symmetry paths in the Brillouin zones were adopted following the conventions used by Setyawan et al.[64]. To examine the extent of localization of the phonon modes, we calculate their phonon PR using the formula[50,65]:

$$P(\omega_q) = \left(\sum_i^N \frac{|e_i(\omega_q)|^2}{M_i} \right)^2 / N \sum_i^N \frac{|e_i(\omega_q)|^4}{M_i^2}, \tag{5}$$

where $e_i(\omega_q)$ is the eigenvector of the phonon mode at wavevector, q with frequency ω, M_i is the mass of the ith atom in the unit cell containing a total number of N atoms. The value of $P(\omega_q)$ ranges between 0 and 1. In an ordered crystal, when $P(\omega_q)$ becomes close to 1, it indicates that the phonon mode is propagative where all the atoms in the unit cell participate. On the other hand, very low values of PR (~0.2)[65,66] indicate the strong localization of the phonon modes (e.g., rattling phonons) where only a few atoms in the unit cell participate in the vibrations. Examples of rattler atoms containing compounds include filled clathrates (Ba_8Si_{46} and $Ba_8Ga_{16}Ge_{30}$)[50,65], where the filler atoms act as ideal rattlers that induce ultralow κ_l in them.

Thermal conductivity calculations

We calculate the κ_l utilizing the phonon lifetimes obtained from the third-order IFCs[67–69], which was shown to reproduce κ_l within 5% of the experimentally measured κ_l in this $AMM'Q_3$ family of compounds[34,35]. We constructed the third-order IFCs of each compound based on DFT calculations of displaced supercell configurations by limiting the cut-off distance (r_c) up to the third nearest neighbor. We used $2 \times 2 \times 1$ supercell (containing 48 atoms) of the primitive unit cell (with 12 atoms) using thirdorder.py[45] utility for the calculation of IFCs. Using the second and third-order IFCs in the ShengBTE code[45], we calculate the temperature-dependent phonon scattering rates and κ_l utilizing a full iterative solution to the PBTE for phonons using a $12 \times 12 \times 12$ q-point mesh. The calculated κ_l generally depends on the r_c which accounts for the maximum range of interaction in the third-order IFCs[52]. It was shown that good convergence of κ_l was obtained by limiting r_c to the third nearest neighbor within the crystal structure in this family of compounds[35].

Calculation of thermoelectric properties

We calculate the TE properties of the four compounds in Table 2, i.e., $BaCuScTe_3$, $BaAgGdSe_3$, $CsZnScTe_3$, $CsCdYTe_3$ to assess their energy conversion efficiencies. We have calculated their electrical transport properties i.e., the Seebeck coefficient (S), power factor ($S^2\sigma$), where σ is the electrical conductivity using the BoltzTrap code[70] within the constant relaxation time approximation, which has been widely used to estimate the themoelectric performance of semiconductors. We have estimated the TE figure-of-merit (ZT) using Eq. (1). While κ_l is calculated using the PBTE, we have determined κ_e employing the Wiedemann–Franz law. BoltzTrap code employs the Boltzmann transport equation (BTE) for electrons to calculate the electrical transport properties. We use a dense $20 \times 20 \times 20$ k-mesh to obtain the electronic band energy which are used in the BoltzTrap code while solving the BTE. Since the compounds in Table 2 have layered crystal structures, we have plotted all TE properties along two crystallographic directions: out-of-plane direction which is parallel (||) to the stacking direction of the layers in the crystal structure and in-plane direction, which is perpendicular (⊥) to the stacking direction. Furthermore, we plot the properties as a function of electron (i.e., n-type doping) and hole (i.e., p-type doping) carrier concentrations. We provide the figures showing the TE properties of those four compounds in the Supplementary Information (Supplementary Figs. 5–8).

The determination of realistic values of the power factor and ZT crucially depends on the electronic relaxation time (τ) and its accurate determination using first-principles quantum mechanical methods are computationally very expensive. Although τ has been calculated for elemental metal[71], binary[72], or even ternary[73] systems with relatively smaller unit cells through determination of the electron-phonon scattering matrix elements using ab initio methods, such calculations become computationally prohibitive for quaternary systems. Hence, the determination of τ using first-principles methods for compounds with quaternary chemistry, such as the family of AMM′Q$_3$ compounds, remains an important yet challenging future work.

It is known that τ in doped semiconductors and metals can vary from few fs (1 fs = 10^{-15} s) to a few tens of fs and shows strong dependence on temperature as well as carrier concentration. For example, from the fit to the experimentally measured electrical conductivity data, Hao et al.[74] showed that τ of SnSe varies from 27 to 4 fs as temperature increases from 300 to 800 K for hole concentrations that change from 4×10^{19} to 6.5×10^{19} cm^{-3}. On the other hand, it was theoretically shown[73] that τ varies from 108 to 6 fs between 300 and 900 K in BaAu$_2$P$_4$. Hence, to get an estimate of the TE performance of the AMM′Q$_3$ compounds considered in this work, here, we take three conservative choices of relaxation times, namely 5, 10, and 20 fs, and evaluate the power factor and ZT of the four compounds (BaCuScTe$_3$, BaAgGdSe$_3$, CsZnScTe$_3$, and CsCdYTe$_3$) at two different temperatures (300 and 600 K). We present the results in Table 2 highlighting the TE performance of these compounds and present their detailed figures (Supplementary Figs. 5–8) in the Supplementary Information.

Finally, we note that the constant relaxation time approximation used in this study assumes that (1) τ for both holes and electrons is independent of the wave vector and energy and (2) all the details of electron scattering (of which the electron-phonon processes are usually the most important) are lumped into the constant, τ. Hence, a large degree of uncertainty may be involved in our assumed values of τ's. As a result, the calculated TE properties, particularly, the power factor and ZT's of the compounds should be taken with caution. A reliable method of estimation of τ would be through the calculations the full electron-phonon matrix elements, which are generally computationally very expensive[71], and hence falls outside the scope of the present work.

Predictive statistical modeling of κ_l

The creation of predictive and transferable model of κ_l is an active field of research. Such a model in principle can be made using machine learning methods such as transfer learning or deep learning. However, like any accurate machine learning model, training a high-quality model requires a large set of high-quality data which is quite scare as the generation of the κ_l data using PBTE or any other first-principles method is computationally prohibitive.

Here, we have made a linear regression model which can be used to predict the κ_l of any AMM′Q$_3$ compound without explicitly doing PBTE calculations. To this end, we calculate bulk (B) and shear (G) moduli of the ten compounds for which we already calculated κ_l using the PBTE (Fig. 5). Utilizing B and G, we calculated the longitudinal (v_L) and transverse (v_T) speed of sounds:

$$\begin{aligned} v_L &= \sqrt{(B + \tfrac{4}{3}G)/\rho} \\ v_T &= \sqrt{G/\rho}, \end{aligned} \tag{6}$$

where ρ is the density of a compound. Next, we calculate the average speed of sound (v_{av}) using the formula[75]:

$$3{v_{av}}^{-3} = {v_L}^{-3} + 2{v_T}^{-3}. \tag{7}$$

We plot the directionally averaged κ_l (at 300 K) against the average speed of sound (v_{av}) for those ten compounds in Fig. 5k. It can be seen that the average κ_l shows almost linear correlation with the average κ_l. Next, we train a linear regression model on these data which form the training set.

We fit a linear regression model, $f(x)$, to the data in Fig. 5k which yields an R^2 value of 0.71, which implies that given the average speed of sound of any AMM′Q$_3$ compound, this model can predict its κ_l with 71% accuracy. Given the very small size of the training data, the performance of the model can be considered to be quite good. To validate this model, we calculate the average speed of sounds and κ_l of another four compounds (BaCuScS$_3$, BaAgYS$_3$, TlCuHfSe$_3$, BaCuYTe$_3$) that belong to the validation set using the DFT and PBTE. Next, we predict their κ_l using the above regression model, compare them with their actual calculated values (at T = 300 K), and estimate the error in prediction: BaCuScS$_3$ (κ_l (actual) = 2.87 Wm^{-1} K^{-1}, κ_l (predicted) = 3.14 Wm^{-1} K^{-1}, error = 9.4%), BaAgYS$_3$ (κ_l (actual) = 1.94 Wm^{-1} K^{-1}, κ_l (predicted) = 2.29 Wm^{-1} K^{-1}, error = 18.0%), TlCuHfSe$_3$ (κ_l (actual) = 1.29 Wm^{-1} K^{-1}, κ_l (predicted) = 1.45 Wm^{-1} K^{-1}, error = 12.4%), and BaCuYTe$_3$ (κ_l (actual) = 1.75 Wm^{-1} K^{-1}, κ_l (predicted) = 1.59 Wm^{-1} K^{-1}, error = 9.1%). Hence, the average error in prediction is 12.3% which falls within the error of the trained regression model. We provide the bulk modulus, shear modulus, speed of sound, κ_l data of the compounds in the training, validation, and test sets in the Supplementary Information in Supplementary Tables 1–3, respectively.

DATA AVAILABILITY

The data that support the findings of the work are in the manuscript and Supplementary Information. The structures and energetics of the predicted compounds would be made available through the Open Quantum Materials database (OQMD) in a future release. Additional data will be available upon reasonable request.

CODE AVAILABILITY

Open-source codes are used throughout this work.

Received: 28 December 2020; Accepted: 23 April 2021;
Published online: 03 June 2021

REFERENCES

1. Curtarolo, S. et al. The high-throughput highway to computational materials design. *Nat. Mater.* **12**, 191 (2013).
2. Mounet, N. et al. Two-dimensional materials from high-throughput computational exfoliation of experimentally known compounds. *Nat. Nanotechnol.* **13**, 246 (2018).
3. Saal, J. E., Kirklin, S., Aykol, M., Meredig, B. & Wolverton, C. Materials design and discovery with high-throughput density functional theory: the open quantum materials database (oqmd). *JOM* **65**, 1501 (2013).
4. Kirklin, S. et al. The open quantum materials database (oqmd): assessing the accuracy of dft formation energies. *npj Comput. Mater.* **1**, 1 (2015).
5. Jain, A. et al. Commentary: the materials project: a materials genome approach to accelerating materials innovation. *Apl. Mater.* **1**, 011002 (2013).
6. Jain, A., Shin, Y. & Persson, K. A. Computational predictions of energy materials using density functional theory. *Nat. Rev. Mater.* **1**, 1 (2016).
7. Meng, Y. S. & Arroyo-de Dompablo, M. E. First principles computational materials design for energy storage materials in lithium ion batteries. *Energy Environ. Sci.* **2**, 589 (2009).
8. Greeley, J., Jaramillo, T. F., Bonde, J., Chorkendorff, I. & Nørskov, J. K. Computational high-throughput screening of electrocatalytic materials for hydrogen evolution. *Nat. Mater.* **5**, 909 (2006).
9. Gautier, R. et al. Prediction and accelerated laboratory discovery of previously unknown 18-electron abx compounds. *Nat. Chem.* **7**, 308 (2015).
10. Zakutayev, A. et al. Theoretical prediction and experimental realization of new stable inorganic materials using the inverse design approach. *J. Am. Chem. Soc.* **135**, 10048 (2013).
11. Anand, S., Wood, M., Xia, Y., Wolverton, C. & Snyder, G. J. Double half-heuslers. *Joule* **3**, 1226 (2019).
12. Wang, J. et al. Exploration of stable strontium phosphide-based electrides: theoretical structure prediction and experimental validation. *J. Am. Chem. Soc.* **139**, 15668 (2017).
13. Xi, L. et al. Discovery of high-performance thermoelectric chalcogenides through reliable high-throughput material screening. *J. Am. Chem. Soc.* **140**, 10785 (2018).
14. Hao, S. et al. Theoretical prediction and experimental confirmation of unusual ternary ordered semiconductor compounds in sr-pb-s system. *J. Am. Chem. Soc.* **136**, 1628 (2014).
15. Samanta, M., Pal, K., Waghmare, U. V. & Biswas, K. Intrinsically low thermal conductivity and high carrier mobility in dual topological quantum material, n-type bite. *Angew. Chem.* **132**, 4852 (2020).
16. Darolia, R. Thermal barrier coatings technology: critical review, progress update, remaining challenges and prospects. *Int. Mater. Rev.* **58**, 315 (2013).
17. Matsunaga, T. et al. Phase-change materials: vibrational softening upon crystallization and its impact on thermal properties. *Adv. Funct. Mater.* **21**, 2232 (2011).
18. Zhao, L.-D. et al. Ultrahigh power factor and thermoelectric performance in hole-doped single-crystal snse. *Science* **351**, 141 (2016).
19. Biswas, K. et al. High-performance bulk thermoelectrics with all-scale hierarchical architectures. *Nature* **489**, 414 (2012).

20. van Roekeghem, A., Carrete, J., Oses, C., Curtarolo, S. & Mingo, N. High-throughput computation of thermal conductivity of high-temperature solid phases: the case of oxide and fluoride perovskites. *Phys. Rev. X* **6**, 041061 (2016).
21. Carrete, J., Li, W., Mingo, N., Wang, S. & Curtarolo, S. Finding unprecedentedly low-thermal-conductivity half-heusler semiconductors via high-throughput materials modeling. *Phys. Rev. X* **4**, 011019 (2014).
22. He, J. et al. Ultralow thermal conductivity in full heusler semiconductors. *Phys. Rev. Lett.* **117**, 046602 (2016).
23. Belsky, A., Hellenbrandt, M., Karen, V. L. & Luksch, P. New developments in the inorganic crystal structure database (icsd): accessibility in support of materials research and design. *Acta Crystallogr. Sect. B: Struct. Sci.* **58**, 364 (2002).
24. Curtarolo, S. et al. Aflowlib. org: a distributed materials properties repository from high-throughput ab initio calculations. *Comput. Mater. Sci.* **58**, 227 (2012).
25. Koscielski, L. A. & Ibers, J. A. The structural chemistry of quaternary chalcogenides of the type amm′q3. *Z. Anorg. Allg. Chem.* **638**, 2585 (2012).
26. Prakash, J., Mesbah, A., Beard, J. C. & Ibers, J. A. Syntheses and crystal structures of baagtbs3, bacugdte3, bacutbte3, baagtbte3, and csagute3. *Z. Anorg. Allg. Chem.* **641**, 1253 (2015).
27. Ruseikina, A., Kol'tsov, S., Andreev, O. & Pimneva, L. Crystal structure of eulnags 3 (ln = gd and ho) compounds. *Rus. J. Inorg. Chem.* **62**, 1632 (2017).
28. Ruseikina, A. V. et al. Synthesis, structure, and properties of euercus3. *J. Alloys Compd.* **805**, 779 (2019).
29. Ruseikina, A. V., Solovyov, L. A., Grigoriev, M. V. & Andreev, O. V. Crystal structure variations in the series srlncus3 (ln = la, pr, sm, gd, er and lu). *Acta Crystallogr. Sect. B: Struct. Sci.* **75**, 584 (2019).
30. Sikerina, N. & Andreev, O. Crystal structures of srlncus 3 (ln= gd, lu). *Russ. J. Inorg. Chem.* **52**, 581 (2007).
31. Maier, S. et al. Crystal structures of the four new quaternary copper (i)-selenides a0. 5cuzrse3 and acuyse3 (a= sr, ba). *J. Solid State Chem.* **242**, 14 (2016).
32. Azarapin, N. O. et al. Synthesis, structural and spectroscopic properties of orthorhombic compounds balncus3 (ln= pr, sm). *J. Alloys Compd.* **832**, 153134 (2020).
33. Strobel, S. & Schleid, T. Three structure types for strontium copper (i) lanthanide (iii) selenides srcumse3 (m= la, gd, lu). *J. Alloys Compd.* **418**, 80 (2006).
34. Hao, S. et al. Design strategy for high-performance thermoelectric materials: The prediction of electron-doped kzrcuse3. *Chem. Mater.* **31**, 3018 (2019).
35. Pal, K., Xia, Y., He, J. & Wolverton, C. Intrinsically low lattice thermal conductivity derived from rattler cations in an amm′q3 family of chalcogenides. *Chem. Mater.* **31**, 8734 (2019).
36. Pal, K., Hua, X., Xia, Y. & Wolverton, C. Unraveling the structure-valence-property relationships in amm′ q3 chalcogenides with promising thermoelectric performance. *ACS App. Energy Mater.* **3**, 2110 (2019).
37. Pal, K., Xia, Y., He, J. & Wolverton, C. High thermoelectric performance in baagyte3 via low lattice thermal conductivity induced by bonding heterogeneity. *Phys. Rev. Mater.* **3**, 085402 (2019).
38. Hautier, G., Jain, A. & Ong, S. P. From the computer to the laboratory: materials discovery and design using first-principles calculations. *J. Mater. Sci.* **47**, 7317 (2012).
39. Sun, W. et al. The thermodynamic scale of inorganic crystalline metastability. *Sci. Adv.* **2**, e1600225 (2016).
40. Aykol, M., Dwaraknath, S. S., Sun, W. & Persson, K. A. Thermodynamic limit for synthesis of metastable inorganic materials. *Sci. Adv.* **4**, eaaq0148 (2018).
41. Jain, A. et al. A high-throughput infrastructure for density functional theory calculations. *Comput. Mater. Sci.* **50**, 2295 (2011).
42. Ward, L. & Wolverton, C. Atomistic calculations and materials informatics: a review. *Curr. Opin. Solid State Mater. Sci.* **21**, 167 (2017).
43. Haastrup, S. et al. The computational 2d materials database: high-throughput modeling and discovery of atomically thin crystals. *2D Mater.* **5**, 042002 (2018).
44. Emery, A. A., Saal, J. E., Kirklin, S., Hegde, V. I. & Wolverton, C. High-throughput computational screening of perovskites for thermochemical water splitting applications. *Chem. Mater.* **28**, 5621 (2016).
45. Li, W., Carrete, J., Katcho, N. A. & Mingo, N. Shengbte: A solver of the boltzmann transport equation for phonons. *Comput. Phys. Commun.* **185**, 1747 (2014).
46. Zhao, L.-D. et al. Ultralow thermal conductivity and high thermoelectric figure of merit in snse crystals. *Nature* **508**, 373 (2014).
47. Wu, D. et al. Direct observation of vast off-stoichiometric defects in single crystalline snse. *Nano Energy* **35**, 321 (2017).
48. Jana, M. K. et al. Intrinsic rattler-induced low thermal conductivity in zintl type tlinte2. *J. Am. Chem. Soc.* **139**, 4350 (2017).
49. Lin, H. et al. Concerted rattling in csag5te3 leading to ultralow thermal conductivity and high thermoelectric performance. *Angew. Chem.* **128**, 11603 (2016).
50. Tadano, T., Gohda, Y. & Tsuneyuki, S. Impact of rattlers on thermal conductivity of a thermoelectric clathrate: a first-principles study. *Phys. Rev. Lett.* **114**, 095501 (2015).
51. Li, W. & Mingo, N. Ultralow lattice thermal conductivity of the fully filled skutterudite ybfe4sb12 due to the flat avoided-crossing filler modes. *Phys. Rev. B* **91**, 144304 (2015).
52. Li, C. W. et al. Orbitally driven giant phonon anharmonicity in snse. *Nat. Phys.* **11**, 1063 (2015).
53. Nielsen, M. D., Ozolins, V. & Heremans, J. P. Lone pair electrons minimize lattice thermal conductivity. *Energy Environ. Sci.* **6**, 570 (2013).
54. Green, M. L. et al. Fulfilling the promise of the materials genome initiative with high-throughput experimental methodologies. *App. Phys. Rev.* **4**, 011105 (2017).
55. Xia, Y., Pal, K., He, J., Ozoliņš, V. & Wolverton, C. Particlelike phonon propagation dominates ultralow lattice thermal conductivity in crystalline tl3vse4. *Phys. Rev. Lett* **124**, 065901 (2020a).
56. Xia, Y. et al. High-throughput study of lattice thermal conductivity in binary rocksalt and zinc blende compounds including higher-order anharmonicity. *Phys. Rev. X* **10**, 041029 (2020).
57. Pal, K., Xia, Y. & Wolverton, C. Microscopic mechanism of unusual lattice thermal transport in tlinte_2. *npj Comput. Mater.* **7**, 1 (2021).
58. Kresse, G. & Furthmüller, J. Efficiency of ab-initio total energy calculations for metals and semiconductors using a plane-wave basis set. *Comp. Mater. Sci.* **6**, 15 (1996).
59. Kresse, G. & Joubert, D. From ultrasoft pseudopotentials to the projector augmented-wave method. *Phys. Rev. B* **59**, 1758 (1999).
60. Perdew, J. P., Burke, K. & Ernzerhof, M. Generalized gradient approximation made simple. *Phys. Rev. Lett.* **77**, 3865 (1996).
61. Cerqueira, T. F. et al. Identification of novel cu, ag, and au ternary oxides from global structural prediction. *Chem. Mater.* **27**, 4562 (2015).
62. Wu, Y., Lazic, P., Hautier, G., Persson, K. & Ceder, G. First principles high throughput screening of oxynitrides for water-splitting photocatalysts. *Energy Environ. Sci.* **6**, 157 (2013).
63. Togo, A. & Tanaka, I. First principles phonon calculations in materials science. *Scr. Mater.* **108**, 1 (2015).
64. Setyawan, W. & Curtarolo, S. High-throughput electronic band structure calculations: challenges and tools. *Comp. Mater. Sci* **49**, 299 (2010).
65. Pailhès, S. et al. Localization of propagative phonons in a perfectly crystalline solid. *Phys. Rev. Lett.* **113**, 025506 (2014).
66. Beltukov, Y., Kozub, V. & Parshin, D. Ioffe-regel criterion and diffusion of vibrations in random lattices. *Phys. Rev. B* **87**, 134203 (2013).
67. Chaput, L., Togo, A., Tanaka, I. & Hug, G. Phonon-phonon interactions in transition metals. *Phys. Rev. B* **84**, 094302 (2011).
68. Togo, A., Chaput, L. & Tanaka, I. Distributions of phonon lifetimes in brillouin zones. *Phys. Rev. B* **91**, 094306 (2015).
69. Zhou, F., Nielson, W., Xia, Y. & Ozoliņš, V. Lattice anharmonicity and thermal conductivity from compressive sensing of first-principles calculations. *Phys. Rev. Lett.* **113**, 185501 (2014).
70. Madsen, G. K. & Singh, D. J. Boltztrap. a code for calculating band-structure dependent quantities. *Comput. Phys. Commun.* **175**, 67 (2006).
71. Xu, B. & Verstraete, M. J. First principles explanation of the positive seebeck coefficient of lithium. *Phys. Rev. Lett.* **112**, 196603 (2014).
72. Song, Q., Liu, T.-H., Zhou, J., Ding, Z. & Chen, G. Ab initio study of electron mean free paths and thermoelectric properties of lead telluride. *Mater. Today Phys.* **2**, 69 (2017).
73. Pal, K., He, J. & Wolverton, C. Bonding hierarchy gives rise to high thermoelectric performance in layered zintl compound baau2p4. *Chem. Mater.* **30**, 7760 (2018).
74. Hao, S., Shi, F., Dravid, V. P., Kanatzidis, M. G. & Wolverton, C. Computational prediction of high thermoelectric performance in hole doped layered gese. *Chem. Mater.* **28**, 3218 (2016).
75. Christensen, M. et al. Avoided crossing of rattler modes in thermoelectric materials. *Nat. Mater.* **7**, 811 (2008).

ACKNOWLEDGEMENTS

K.P. and C.W. acknowledge support from the U.S. Department of Energy under Contract No. DE-SC0014520 (thermal conductivity calculations) and the Center for Hierarchical Materials Design (CHiMaD) and from the U.S. Department of Commerce, National Institute of Standards and Technology under Award No. 70NANB14H012 (HT-DFT calculations). J.S. and J.H. acknowledge support from the National Science Foundation through the MRSEC program (NSF-DMR 1720139) at the Materials Research Center (phase stability). Y.X. acknowledges support from Toyota Research Institute (TRI) through the Accelerated Materials Design and Discovery program (lattice dynamics). Y.L. and M.G.K. were supported in part by the National Science Foundation Grant DMR-2003476. K.P. sincerely thanks Sean Griesemer for useful discussion on the abundance of various crystallographic prototypes in the OQMD. We acknowledge the computing resources provided by (1) the National Energy Research Scientific Computing Center (NERSC), a U.S. Department of Energy Office of Science User Facility operated under Contract No. DE-AC02-05CH11231, (2) Quest high-performance computing facility at Northwestern University which is jointly supported by the Office of the Provost, the Office for Research, and Northwestern University Information Technology, and (3) the Extreme Science and Engineering Discovery Environment (National Science Foundation Contract ACI-1548562).

AUTHOR CONTRIBUTIONS

K.P. conceived and designed the project. K.P. performed calculations and analysis with help and suggestions from Y.X., J.S., J.H., Y.L., M.G.K., and C.W. C.W. supervised the whole project. All authors discussed the results, provided comments, and contributed to writing the manuscript.

COMPETING INTERESTS

The authors declare no competing interests.

ADDITIONAL INFORMATION

Supplementary information The online version contains supplementary material available at https://doi.org/10.1038/s41524-021-00549-x.

Correspondence and requests for materials should be addressed to K.P. or C.W.